

Point Clouds Denoising Method Based on SPAD Discrete Probability Model and Completion

Chengzhi Qu^{ID}, Yan Zhang^{ID}, Ziwen Sun^{ID}, Feifan Ma^{ID}, and Xin Zhang^{ID}

Abstract—The laser imaging system based on single-photon avalanche diodes (SPADs) has demonstrated significant promise in long-range or low-power detection. However, the obtained point clouds encompass intricate noise attributable to the device's detection characteristics, significantly affecting downstream applications. In this article, we present a novel denoising method named LCLOF for SPAD-acquired point clouds, built upon a completion denoising strategy and the SPAD discrete detection probability model. Instead of directly denoising the input raw data, LCLOF outputs clean data through point cloud completion. Specifically, the proposed method involves preprocessing the input data to extract feature points and incomplete point clouds. The SPAD discrete probability model is integrated into point cloud preprocessing to achieve the desired outcome. Moreover, an improved local outlier factor (ILOF) approach is put forth as the completion strategy. Denoising will be accomplished by using ILOF to filter out feature points and fill the incomplete point clouds. Theoretical analysis illustrates the feasibility of the completion strategy in scenarios involving point clouds with nonuniform density. Experimental results illustrate the performance of the proposed method over state-of-the-art approaches concerning the denoising of point clouds in the context of SPAD-based laser imaging system.

Index Terms—Completion denoising, discrete detection probability model, point clouds denoising, single-photon avalanche diode (SPAD).

I. INTRODUCTION

THE laser imaging system based on single-photon avalanche diodes (SPADs) can capture point clouds with faint signals due to its heightened sensitivity, which finds extensive applications, including remote sensing, underwater imaging, space exploration, and biological imaging [1], [2], [3]. Its exceptional performance results in a considerable extension of the achievable measurement distance, and permits the utilization of low-power laser sources in situations where device power consumption needs to be constrained [4].

Manuscript received 4 September 2023; revised 5 December 2023 and 17 January 2024; accepted 2 February 2024. Date of publication 9 February 2024; date of current version 16 February 2024. (Corresponding author: Yan Zhang.)

Chengzhi Qu is with the School of Artificial Intelligence, Nanjing University of Information Science and Technology, Nanjing 211544, China (e-mail: 003791@nuist.edu.cn).

Yan Zhang is with the School of Electronics and Communication Engineering, Sun Yat-sen University, Shenzhen Campus, Shenzhen 518063, China (e-mail: zhangyan25@mail.sysu.edu.cn).

Ziwen Sun and Feifan Ma are with the School of Aeronautics and Astronautics, Sun Yat-sen University, Shenzhen Campus, Shenzhen 518063, China (e-mail: sunzw3@mail2.sysu.edu.cn; maff@mail2.sysu.edu.cn).

Xin Zhang is with the Shanghai Satellite Engineering Institute, Shanghai 201111, China (e-mail: zxzhangxin0@163.com).

Digital Object Identifier 10.1109/TGRS.2024.3364252

However, a fundamental drawback is that the point clouds acquired by this high-sensitivity equipment will inherently contain substantial background noise. Removing noise from raw point clouds remains a challenging task [5], [6].

Some researchers have proposed a variety of denoising methods for point clouds, which can be divided into two categories: noise removal methods and noise restoration methods [7]. Noise removal methods involve single-level or multilevel processing of the input raw point clouds using strategies based on local characteristics [8]. The denoising task is achieved through the detection and removal of noise points. Noise restoration methods consider noise points as shifts from truth points and use a denoising strategy to smooth the input point clouds, yielding clean point clouds [9]. Furthermore, noise restoration methods can be employed for noise removal, utilizing the calculated shifts as the basis for assessment.

However, point clouds acquired via SPAD-based laser imaging systems frequently exhibit substantial distortion, and the noise points' density also varies considerably [10]. Existing denoising methods either remove the noise directly by extracting features in one or more steps from the raw point clouds, or calculate point position updates to obtain clean point clouds. However, there are three limitations: 1) these methods cannot handle complex noise present in SPAD-acquired point clouds obtained from real-world scenes; 2) the embedding of iterative calculation enhances the accuracy of noise point identification, but it incurs significant time costs, leading to low practicality; and 3) in our previous work, a completion-based point clouds denoising method is proposed to remove noise by filling in incomplete point clouds [11], which has been proved to be effective for synthetic point clouds. However, it still struggles to achieve satisfactory denoising results for SPAD-acquired point clouds.

To solve the above problems, we propose a completion denoising method named LCLOF with the consideration of the SPAD discrete probability model and the improved local outlier factor (ILOF). The proposed method consists of three parts: rough-denoising, over-denoising, and point cloud completion. Rough-denoising generates rough point clouds in the form of filtering the input raw data. Over-denoising produces incomplete point clouds based on the rough point clouds. These two procedures are designed with the consideration of the SPAD discrete probability model to obtain the desired output and enhance denoising efficiency. Feature points are then generated by calculating the difference between incomplete point clouds and rough point clouds. Clean point clouds

are obtained by filling incomplete point clouds with filtered feature points. Additionally, we introduce ILOF as the filtering strategy for completion denoising. ILOF selects only the incomplete point clouds to construct the nearest neighbor set, providing more precise local characteristics for the filtering of feature points. We also provide theoretical analysis to demonstrate that ILOF is applicable for the filtering of points with nonuniform density. Using synthetic data and real-world data scanned by SPAD-based laser imaging systems, the experimental results show the superiority of the proposed technique over state-of-the-art methods. The main contributions of this article can be summarized as follows.

- 1) We propose a novel denoising method for SPAD-acquired point clouds, which relies on a completion denoising strategy and incorporates the discrete detection probability model of SPAD.
- 2) ILOF is formulated to execute the completion process, considering the density correlation between incomplete point clouds and feature points. Theoretical analysis is also proposed to prove the feasibility of ILOF.
- 3) In comparison to the state-of-the-art methods, experimental results obtained from both synthetic and real-world scanned point clouds substantiate that the proposed method attains superior performance.

The organization of this article is as follows. In Section II, a review of recent research is presented. Section III encompasses the analysis of the imaging model. Section IV presents the framework of the proposed method. Section V displays and evaluates the outcomes of experiments. Section VI encapsulates the conclusions.

II. RECENT WORK

In this part, the noise removal methods are reviewed first, then the noise restoration methods are discussed.

A. Noise Removal Methods

Previous denoising methods for noise removal can be divided into three categories: statistics-based methods, density-based methods, and spatial-based methods.

Statistics-based methods employ the statistical characteristics of nearest neighbor points as the foundation for noise detection. The statistical outlier removal (SOR) method is a typical statistics-based strategy for point cloud noise removal [8]. In SOR, the mean distance between each point and its neighboring points is considered as the neighbor distance. Statistical results of these neighbor distances are utilized for the purpose of noise point detection. In order to effectively process extensive point clouds, a rapid clustering SOR technique was proposed that introduces clustering operations to expedite the denoising process calculations [13]. However, this class of methods plays poor performance for point clouds with high noise proportion.

Density-based methods use density information to realize denoising. The local outlier factor (LOF) method introduces the concept of relative density for denoising point clouds. Local density in LOF is computed by assessing the reachable distance between each point and its neighboring points [14]. The noise score is defined as the ratio of the local density

of each point to the average local density of its neighboring points. The connectivity-based LOF method introduces the concept of isolation to characterize the similarity between points, quantifying it through the calculation of the chain distance of neighboring points [15]. Ning et al. [16] proposed an efficient denoising method for 3-D scanning imaging LiDAR, involving the analysis of local density. Noisy points are eliminated using a local density threshold. Density-based methods are less affected by the proportion of noise, but the corresponding denoising accuracy is lower.

Spatial-based methods accomplish denoising based on the spatial correlation of nearest neighbor points. Zhou et al. [17] proposed a noniterative layered method by dividing denoising process into two stages: small threshold and large threshold. Each stage performs layered denoising on point clouds with different threshold ranges. The layered denoising strategy circumvents the computationally expensive operation of neighbor point retrieval, but cannot effectively address point clouds with nonuniform density. Multiple denoising methods are proposed by using the pulsewidth to distinguish the signal and noise based on the correlation characteristics of neighboring photons [10], [18], [19]. These denoising methods consider the characteristics of laser detection, but the processing effectiveness for SPAD-acquired point clouds remains less than ideal.

B. Noise Restoration Methods

Currently, the mainstream point cloud noise restoration methods can be divided into three categories: filter-based methods, optimization-based methods, and deep learning-based methods.

Filter-based noise restoration methods primarily originate from the field of image processing, with representative methods being the bilateral filtering methods and guided filtering methods. The bilateral filtering methods are nonlinear filtering approaches that achieve noise reduction and smoothing of point clouds by performing a weighted average considering distance information, normal vector information, or color information of neighboring points [20]. The guided filtering methods assume that noise points in the input point clouds are linear translations of truth points. By extracting local spatial geometry relationships of points, the filtering output point clouds are represented as a linear model of the guided point clouds [21], [22]. Linear model parameters are obtained by minimizing a cost function to achieve point cloud recovery. Filter-based noise restoration methods have a simple structure, but they face challenges in accurately estimating the offset of noise points in sharp feature regions.

Optimization-based noise restoration methods treat the denoising process as an optimization problem, utilizing prior information about the distribution characteristics as constraints to search for smooth point clouds that can approximate the input point clouds. These methods can be divided into four categories: moving least squares-based methods (MLS), local optimal projection-based methods (LOP), sparsity-based methods, and nonlocal-based methods [23]. MLS methods use the input point clouds to approximate a smooth surface, iteratively projecting noise points onto the approximate surface [24]. LOP methods do not explicitly acquire the

approximate surface. Instead, they generate a set of points to approximate the surface, guided by two cost functions: the data term and the repulsion term [25]. These methods minimize the data term cost function to project a set of points onto the approximate surface of the input data. The optimization of the repulsion term cost function enforces uniform distribution of projected points. The core of sparsity-based methods lies in the assumption of local planarity, where the point clouds are assumed to be piecewise smooth [26]. Methods of this category initially solve a global minimization problem to obtain a sparse reconstruction of surface normal. Subsequently, based on the reconstructed normal and the local planar assumption, cost functions are optimized to update the positions of noise points. Nonlocal methods extend the concept of nonlocal self-similarity from image denoising to point cloud processing [27], [28]. They effectively preserve the overall geometric structural features of point clouds during the noise restoration process, making them the current mainstream noise point restoration methods. Nonlocal methods typically divide the point clouds into multiple blocks and achieve restoration based on the similarity of these blocks. Optimization-based methods exhibit notable restoration effects, yet they generally involve multiple parameters and complex computations.

Deep learning-based methods can learn the corresponding mapping from noise points to truth points and denoise input point clouds. One such approach is PointCleanNet, introduced by [29], which is a two-stage point cloud denoising network built upon the PCPNet architecture. This network initially identifies and eliminates noise from the input point clouds, followed by the smoothing of the remaining points. Another method, proposed in [30], involves an encoder-decoder model. The encoder learns potential feature vectors of the input point set, while the decoder decodes the coordinate offsets of 3-D points based on the feature vectors, enabling point cloud filtering and potential noise removal. Presently, deep learning-based methods used for point cloud denoising predominantly rely on supervised learning. These methods yield satisfactory denoising outcomes when provided with abundant training data and ample training time. However, if the point clouds to be denoised significantly deviate from the training data, these methods often struggle to accomplish the denoising task effectively. In addition, the prevailing noise restoration methods frequently rely on synthetic point clouds for validation, which proves challenging in addressing the complex noise present in point clouds acquired from SPAD-based laser imaging systems.

III. IMAGING MODEL ANALYSIS

The schematic of a typical SPAD-based laser imaging system is illustrated in Fig. 1. Laser pulses perform repetitive scans on the target, and the reflected photons are captured by the SPAD sensor, exhibiting a time-of-flight (TOF) of Δt [31]. The distance between the laser imaging system and the target is estimated by

$$L = c \frac{\Delta t}{2} \quad (1)$$

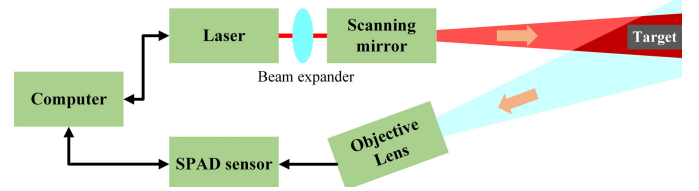


Fig. 1. Schematic of a typical SPAD-based laser imaging system.

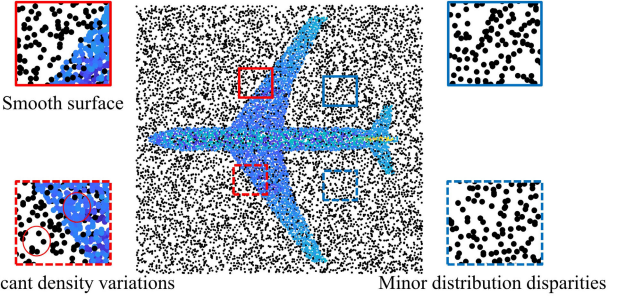


Fig. 2. Analysis of synthetic point clouds.

where c is the speed of light. The computer translates distance information into the 3-D coordinates of each point, taking into account the relevant deflection angle of the scanning mirror. These data obtained from numerous laser scans eventually coalesce into point clouds representing the target. First-photon timing remains the prevailing detection mode in SPAD-based laser imaging systems, wherein it records solely the first detected photon within a specific time interval (the gate time) [32]. However, the first photon is often likely to be a background light photon when the laser imaging system operates outdoors. Low signal-to-noise ratio (SNR) is the characteristic state of point clouds acquired under first-photon timing mode [33].

The distribution of point clouds acquired by the SPAD-based single-photon laser imaging system diverges significantly from that of synthetic point clouds. The ground truth of synthetic point clouds is generally produced by randomly discretized sampling from simulated CAD model surfaces, with noise points introduced by adding varying proportions of noise within the model's bounding box [29]. As shown in Fig. 2, the density difference between ground truth and noise points is apparent in synthetic point clouds. The surface of ground truth exhibits smoothness, while the noise points considerably affect the surface patches. Additionally, the distribution variation of noise across different regions is minimal. Fig. 3 illustrates the visual comparison of the ground truth between synthetic point clouds and point clouds obtained through the SPAD-based laser imaging system. It is evident from Fig. 3(a) that the ground truth of the synthetic point clouds exhibits a uniform distribution. Consequently, the extraction of spatial distribution features, such as normal vectors, density, statistical distances, etc., becomes more accurate. Due to the pronounced distinction in spatial distribution characteristics between ground truth and noise, existing denoising methods can offer a notable effect for synthetic point clouds.

Fig. 4 presents the outcomes of the characteristics analysis for the SPAD-acquired point clouds. As illustrated in the figure, the density difference between ground truth and noise

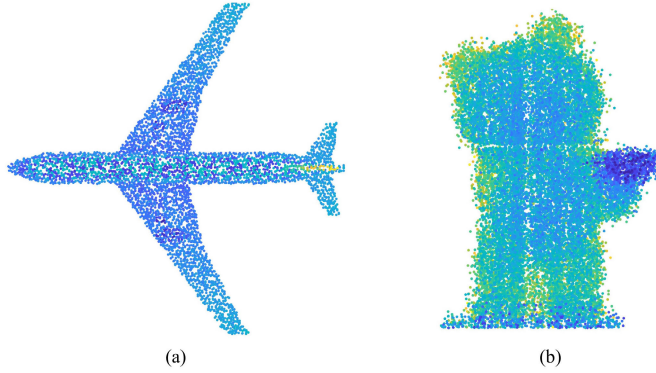


Fig. 3. Visual comparison of the ground truth. (a) Synthetic point clouds. (b) Point clouds obtained through the SPAD-based laser imaging system.

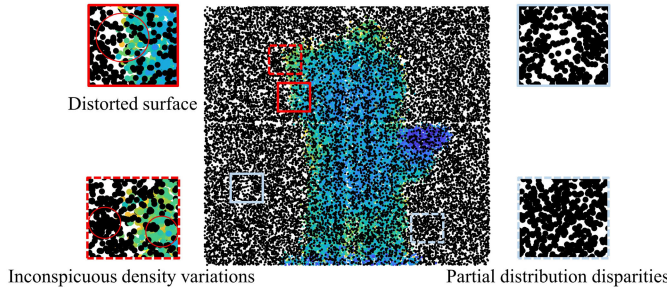


Fig. 4. Analysis of raw point clouds acquired by SPAD-based laser imaging system.

points is nearly imperceptible in some areas. This phenomenon arises due to the influences of factors such as the transmission medium, laser pulsedwidth, target reflection characteristics, and equipment anomalies, resulting in pronounced distortions on the surface of the ground truth within the SPAD-acquired point clouds. Meanwhile, variations in noise distribution can be observed across different regions. As shown in Fig. 3(b), the ground truth distribution of the SPAD-acquired point clouds is nonuniform, which can introduce interference into the feature extraction process.

Furthermore, based on the analysis results in Fig. 4, noise in SPAD-acquired point clouds can be categorized into two types: isolated noise, and nonisolated noise. Isolated noise consists of points with high density and separation from the ground truth. Nonisolated noise is mixed with the ground truth, making it difficult to distinguish from the truth points. In addition, the complex characteristics of SPAD-acquired point clouds make it challenging for existing denoising methods to accurately remove these two types of noise.

IV. DEVELOPMENT OF THE PROPOSED METHOD

Our method extends the previous work [11] to the denoising of SPAD-acquired point clouds. The framework of the proposed method is shown in Fig. 5. Given input noisy point clouds gathered using the SPAD laser imaging system, our approach can yield results of high quality. The proposed method involves the ensuing three steps.

Rough-Denoising: We design a rough-denoising procedure based on the statistical characteristics of local points and SPAD discrete probability model. The primary objective of rough-denoising is to eliminate

substantial isolated noise inherent in the raw data. Throughout this phase, the conservation of target features is prioritized. The generation of rough point clouds post-denoising may still contain residual noise.

Over-Denoising: We establish a layered over-denoising procedure to further process rough point clouds. The adaptive adjustment of noise recognition boundaries within each layer aligns with the SPAD trigger characteristics, enhancing the precision of noise removal. Throughout this procedure, a maximal amount of non-isolated noise will be removed from the rough point clouds, even if it entails sacrificing some target features.

Point Clouds Completion: Feature points are constructed in this procedure, subsequently subjected to filtration, and serve as candidates for filling incomplete point clouds. We introduce an ILOF method as the feature point filtration mechanism, accompanied by the presentation of theoretical analysis.

The details of the proposed method are described as follows.

A. Rough-Denoising

The discrete probability model of SPAD can calculate the sensor's detection probability using the mean number of photoelectrons as a basis, which could offer viable guidance for developing denoising techniques [12]. In the SPAD discrete probability model, the gate time t_{gate} is divided into I intervals, each of length T_a . The triggering of the SPAD depends on the creation of photoelectrons, which is assumed to follow the Poisson distribution [12]. Then, the probability that $K_a(i)$ photoelectrons are generated at the i th interval is given by

$$P_{\text{PE}}(K_a(i), i) = \frac{1}{K_a(i)!} (\bar{K}_a(i))^{K_a(i)} e^{-\bar{K}_a(i)} \quad (2)$$

where $\bar{K}_a(i)$ is the mean number of $K_a(i)$. Hence, the probability that there are no photoelectrons at the i th interval is given by

$$P_{\text{PE}}(0, i) = e^{-\bar{K}_a(i)}. \quad (3)$$

Considering the long-dead time case that the sensor can only be triggered once during the gate time, let the triggering event be denoted as $P_{\text{PE}}(K_a(i) \geq 1, i)$, the probability that the triggering event occurs at the i th interval is given by

$$\begin{aligned} P_{\text{PE}}(K_a(i) \geq 1, i) &= (1 - P_{\text{PE}}(0, i)) \prod_{j=1}^{i-1} P_{\text{PE}}(0, j) \\ &= (1 - e^{-\bar{K}_a(i)}) \prod_{j=1}^{i-1} e^{-\bar{K}_a(j)}. \end{aligned} \quad (4)$$

Assuming the mean number of noise photoelectrons in each interval is \bar{K}_n , the signal reaches the sensor at the i th interval, and the mean number of signal photoelectrons in the i th interval is $\bar{K}_s(i)$. Based on (4), the detection probability in the i th interval is defined as

$$P_s(i) = \left(1 - e^{-\bar{K}_s(i) - \bar{K}_n}\right) \prod_{j=1}^{i-1} e^{-\bar{K}_n}. \quad (5)$$

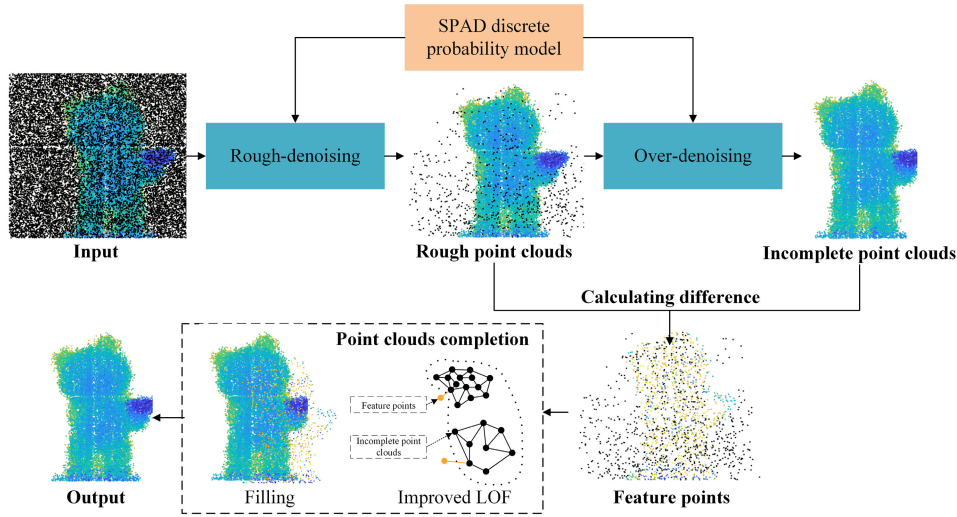


Fig. 5. Framework of the proposed point cloud denoising methods.

In the procedure of rough-denoising, we first estimate the mean number of noise photoelectrons that can be used to assist in calculating the detection probability. A set of point clouds (called full noise point clouds) is collected in the same environment as the input noisy point clouds, which are made up of noise entirely. There are several ways to acquire full noise point clouds such as adjusting the direction of laser illumination so that it is outside the field of view of the lens. Assuming that the number of laser emission pulses is M_{laser} , the points number of the full noise point clouds is M_n ($M_n < M_{\text{laser}}$). According to (3) and (4), the probability that there are no noise photoelectrons during the gate time is given by

$$P_{\text{PE}}(0, I) = \frac{M_{\text{laser}} - M_n}{M_{\text{laser}}} = \prod_{j=1}^I e^{-\bar{K}_n} \quad (6)$$

where \bar{K}_n is the mean number of noise photoelectrons during the gate time and can be given by

$$\bar{K}_n = -\log\left(\frac{M_{\text{laser}} - M_n}{M_{\text{laser}}}\right)/I. \quad (7)$$

In addition, assuming that the noise photoelectrons mainly come from the background light, \bar{K}_n can be calculated by (8) when the full noise point clouds cannot be obtained [34]

$$\bar{K}_n = I_{\text{sun}} \frac{\lambda}{hc} \varphi \theta^2 \rho k_R k_M k'_M A \gamma \eta T_a \quad (8)$$

where I_{sun} is the spectral irradiance of the Sun at the top of the atmosphere, λ is the wavelength of the laser, φ is the diffuse reflection angle of incoming sunlight from the target surface, θ is the angle of view of the sensor, h is Planck's constant, c is the speed of light, ρ is the reflectivity, k_R is the lens loss, k_M is the atmosphere propagation loss between sensor and target, k'_M is the atmosphere propagation loss between Sun and target, A is the area of the receiving telescope, γ is the effective sensor fill factor, η is the quantum efficiency of SPAD.

Considering the input raw point clouds $P = \{p_i, i = 1, 2, \dots, N\}$, $p_i \in R^{1 \times 3}$. Assuming that p_i is a

truth point, then the mean number of signal photoelectrons can be calculated according to the laser radar equation [34]

$$\bar{K}_s(p_i) = E \frac{\lambda}{hc} \rho k_R k_L k_M^2 \frac{A}{R_i^2} \gamma \eta = \frac{\alpha}{R_i^2} \quad (9)$$

where E is the single-pulse laser energy, k_L is the loss of the transmitter optics, R_i is the z -axis coordinate of p_i .

Define k_1 nearest neighbors of p_i as the subset $\{p_j\}_{j=1}^{k_1}$. We calculate the mean number of photoelectrons for p_j based on the relative distance between p_i and p_j

$$\bar{K}_s(p_j) = \frac{\alpha}{d_{ij}^2} \quad (10)$$

where d_{ij} is the Euclidean distance between p_i and p_j . The triggered interval of p_j is given by

$$I_j = \frac{2d_{ij}}{cT_a}. \quad (11)$$

According to (5), if the sensor intends to be triggered in the interval of I_j , the probability of this event is

$$P_s(I_j) = \left(1 - e^{-\bar{K}_n - \bar{K}_s(p_j)}\right) \prod_{l=1}^{I_j-1} e^{-\bar{K}_n}. \quad (12)$$

The average function is applied to map the trigger probability onto a noise score of p_i

$$S_i = \frac{1}{k_1} \sum_{j=1}^{k_1} P_s(I_j). \quad (13)$$

Points will be regarded as noise if their scores are greater than the threshold ψ . Rough-denoising can lead to the generation of rough point clouds. The rough point clouds need to retain feature information as much as possible while allowing for the presence of residual noise points.

B. Over-Denoising

In the procedure of over-denoising, an improved layered method is introduced to process rough point clouds and generate incomplete point clouds. The incomplete point clouds

do not require consideration for feature preservation but must be devoid of noise points. We first divided the input rough point clouds into h hierarchies along the Z -axis

$$h = \frac{|z_{\max} - z_{\min}|}{T_p} \quad (14)$$

where z_{\min} is the lower bound of the input points' Z -axis coordinate, z_{\max} is the upper bound, T_p is the pulselength of the laser.

We establish bounding boxes for each point within each layer. Points will be identified as noise if the number of its nearest neighbors in the box is less than threshold k_2 . Based on (5), it can be seen that the signal detection capacity of SPAD decays with the increase of the distance between the sensor and the target. Therefore, layers that are situated at greater distances from the sensor exhibit a higher degree of sparsity in their point density. To solve this problem, we employ the discrete probability model of SPAD to estimate the side length of bounding boxes for points in each layer. Considering the Z -axis coordinate of the bottom point in each layer is z_{flag} , which is approximated as the distance between the bottom point and the sensor. The corresponding triggered interval and mean number of signal photoelectrons can be calculated by

$$\begin{cases} I_{\text{flag}} = \frac{2z_{\text{flag}}}{cT_a\alpha} \\ \bar{K}_{s-\text{flag}} = \frac{w}{z_{\text{flag}}^2} \end{cases} \quad (15)$$

The side length of bounding boxes for points in each layer is defined as follows:

$$\zeta = \frac{w}{P_{s-\text{flag}}} \quad (16)$$

where $P_{s-\text{flag}}$ is the trigger probability that can be calculated from (12) and (15), w is the bounding threshold.

C. Point Clouds Completion

Assuming the rough point clouds are P' , and the incomplete point clouds are P'' . We define the difference between P' and P'' as feature points: $F = P' - P''$. The LOF method is a well-known outlier detection approach. It calculates the relative density of each data point, and gets the LOF value of each point to determine whether it is an outlier. In this article, ILOF is proposed to filter feature points. Some assumptions of ILOF are defined as follows.

Definition 1: Nearest neighbor. For point $p \in F$, its nearest neighbor set $\{q_i\}_{i=1}^{k_3} \in P''$. For point $q \in P''$, its nearest neighbor set $\{o_i\}_{i=1}^{k_3} \in P''$.

Definition 2: k -distance of point $q \in P''$. The distance between point q and its k_3 th nearest neighbor, denoted as $\text{kdist}(q)$.

Definition 3: Reachability distance of a point. For points $p \in F$ and $q \in P''$, the reachability distance is defined by

$$\text{rdist}(p, q) = \max\{\text{kdist}(q), d(p, q)\} \quad (17)$$

where $d(\cdot)$ is the Euclidean distance between two points.

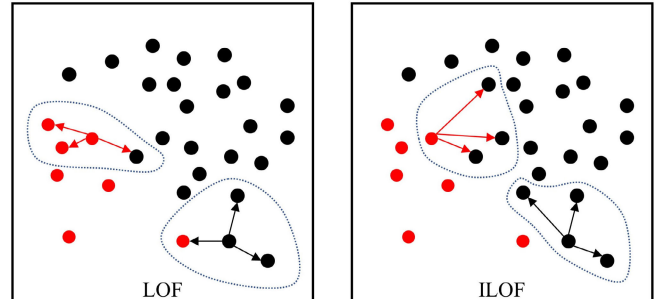


Fig. 6. Visual comparison of nearest neighbor selection between LOF and ILOF.

Definition 4: Local reachability density of a point. The local reachability density of point $p \in F$ is defined as

$$\text{lrd}(p) = \frac{k_3}{\sum_{q \in \{q_i\}_{i=1}^{k_3}} \text{rdist}(p, q)}. \quad (18)$$

The local reachability density of point $q \in P''$ is defined as

$$\text{lrd}(q) = \frac{k_3}{\sum_{o \in \{o_i\}_{i=1}^{k_3}} \text{kdist}(o)}. \quad (19)$$

Definition 5: ILOF value of point $p \in F$. The ILOF value of any feature point is defined as

$$\text{ILOF}(p) = \left| \left(\sum_{q \in \{q_i\}_{i=1}^{k_3}} \frac{\text{lrd}(q)}{\text{lrd}(p)} \right) / k_3 - 1 \right|. \quad (20)$$

Points will be retained to fill incomplete point clouds if their ILOF values are less than threshold δ . The traditional LOF method assigns an outlier score to each point in the dataset to perform outlier detection. The magnitude of this score depends on the degree of isolation of the object relative to its surrounding nearest neighbors. As shown in Fig. 6, the nearest neighbors for each point in LOF are determined globally across the entire dataset. Due to the presence of noise in feature points, this can interfere with LOF's assessment of isolation. In ILOF, the nearest neighbors for each point in both feature points and the incomplete point clouds are derived from the incomplete point clouds. As the incomplete point clouds contain minimal noise, the nearest neighbors in ILOF can provide more authentic local structural information for the targets. Additionally, we provide theoretical analysis to demonstrate the suitability of ILOF for feature point filtering in point clouds with nonuniform density.

D. Theoretical Analysis

Theorem 1: Let d_{\min} denotes the minimum distance, i.e., $d_{\min} = \min\{\text{kdist}(q), d(p, q), \text{kdist}(o) | p \in F, q, o \in P''\}$. Similarly, let d_{\max} denote the maximum distance. Let σ be defined as (d_{\max}/d_{\min}) . Then we have

$$\lim_{\sigma \rightarrow 1} \text{ILOF}(p) = 0. \quad (21)$$

Proof: For all nearest neighbors $q \in P''$ of $p \in F$, the reachability distance is

$$\text{rdist}(p, q) \geq d_{\min} \quad (22)$$

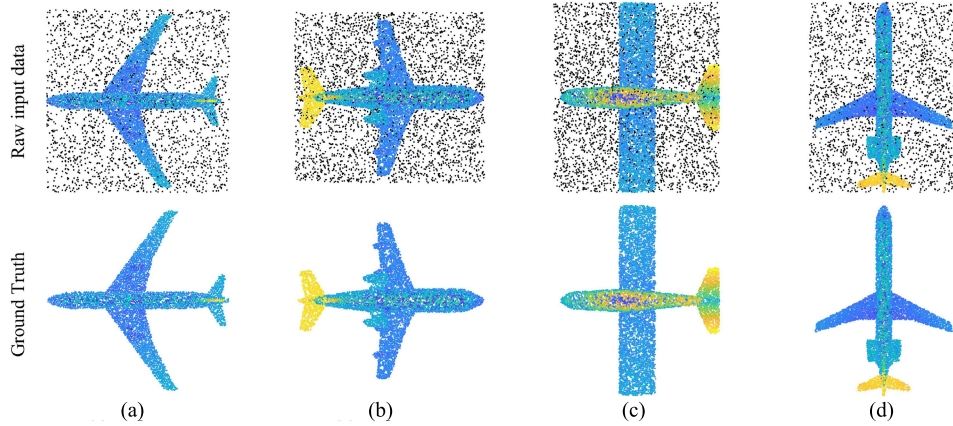


Fig. 7. Models of the synthetic data. (a) Airplane1. (b) Airplane2. (c) Airplane3. (d) Airplane4.

$$\text{rdist}(p, q) \leq d_{\max}. \quad (23)$$

According to (18) and (19), the local reachability density is

$$\begin{cases} 1/d_{\max} \leq \text{lrd}(p) \leq 1/d_{\min} \\ 1/d_{\max} \leq \text{lrd}(q) \leq 1/d_{\min}. \end{cases} \quad (24)$$

The mean local reachability density of $\text{lrd}(q)$ is

$$1/d_{\max} \leq \frac{\sum_{q \in \{q_i\}_{i=1}^{k_3} \text{lrd}(q)}}{k_3} \leq 1/d_{\min}. \quad (25)$$

The relationship between the local reachability of point p and the mean local reachability density of point q is as follows:

$$d_{\min}/d_{\max} \leq \frac{\sum_{q \in \{q_i\}_{i=1}^{k_3} \text{lrd}(q)}}{k_3 \cdot \text{lrd}(p)} \leq d_{\max}/d_{\min}. \quad (26)$$

Thus, it follows that:

$$\lim_{d_{\max}/d_{\min} \rightarrow 1} \frac{\sum_{q \in \{q_i\}_{i=1}^{k_3} \text{lrd}(q)}}{k_3 \cdot \text{lrd}(p)} = 1. \quad (27)$$

According to (20), we have

$$\lim_{\sigma \rightarrow 1} \text{ILOF}(p) = \lim_{\sigma \rightarrow 1} \left| \frac{\sum_{q \in \{q_i\}_{i=1}^k \frac{\text{lrd}(q)}{\text{lrd}(p)}}}{k_3} - 1 \right| = 0. \quad (28)$$

□

Theorem 1 is proved. So, let us consider that $\sigma \rightarrow 1$ is met, which means that the values of $d(p, q)$, $\text{kdist}(q)$, and $\text{kdist}(o)$ are quite close, i.e., the distance between $p \in F$ and $q \in P''$ conforms to the local distribution of q in the incomplete point clouds P'' . If the local distribution of q is tight, a lower $\text{ILOF}(p)$ means that p is also closer to q . In turn, if the local distribution of q is loose, a greater $d(p, q)$ will result in a lower $\text{ILOF}(p)$. This feature enables ILOF to have better capability for the feature points filtering of SPAD-acquired point clouds with uneven density distribution.

V. EXPERIMENTAL RESULTS

A. Test Conditions

In this article, three evaluation metrics have been employed to evaluate the performance of the proposed method [35]. Specifically, the outlier detection rate (ODR) is introduced to quantify the proportion of eliminated noise points relative to

the total number of noise points. The recall rate (Recall) is introduced to evaluate the ability of the methods to retain features, and it is calculated as the ratio of removed noise points to the overall number of points removed. Furthermore, Accuracy is measured based on the agreement between ODR and recall rate. The definitions of these metrics are as follows:

$$\text{ODR} = \frac{N_T}{N_T + N_F} \quad (29)$$

$$\text{Recall} = \frac{N_T}{N_T + R_F} \quad (30)$$

$$\text{Accuracy} = \frac{N_T + R_T}{N_T + N_F + R_T + R_F} \quad (31)$$

where N_F is the number of residual noise points, R_F is the number of removed truth points, N_T is the number of removed noise points, R_T is the number of residual truth points.

We validate the effectiveness of the proposed method using four aircraft models from the synthetic dataset Modelnet40 [36]. To intentionally simulate realistic scenarios, we introduced Poisson distribution noise to these models after downsampling. These models corresponding to the synthetic data are shown in Fig. 7. Furthermore, we carried out denoising experiments on real-world data scanned by the SPAD imaging system to highlight the practical application of our approach. The main parameters of the SPAD imaging system can be seen in Table I. Labels in the scanned point clouds were established by manual annotation, leveraging human visual judgment. The models corresponding to the scanned data are visually depicted in Fig. 8. The specific parameters associated with all experimental data are itemized in Table II.

We compare the denoising results with the SOR method [8], the Local density method [16], the PointCleanNet method [29], the Noniterative method [17], the maximum consistency with minimum distance (MCMD) method [5], the fast depth imaging denoising (FDID) method [10], and the CIMD method [11].

B. Performance Evaluation on Synthetic Data

The visual comparison of denoising outcomes on synthetic data is depicted in Figs. 9–12. It is evident from these figures that the denoising performance of SOR and Local density is poor. A significant number of noise points persist in the results

TABLE I
PARAMETERS SUMMARY OF THE SPAD IMAGING SYSTEM

| System Parameter | Value/Comment |
|-------------------------|---|
| Laser | Pulsed microchip laser with an electrical driver (RealLight MCH-532-10-005) |
| Laser Repetition Rate | 10kHz |
| Illumination Wavelength | 532nm |
| Single Pulse Energy | 5μJ |
| Laser Pulse Width | 300ps full width at half maximum |
| Beam Expander | GCO-140113 Φ40 8x 532nm |
| Objective Lens | Customized receiving telescope Φ90 |
| Scanning Mirror | Galvo Scanning System with Silver-Coated Mirrors (GVS012, Thorlabs) |
| SPAD Sensor | Single Photon Detectors (SPCM50A/M, Thorlabs) |

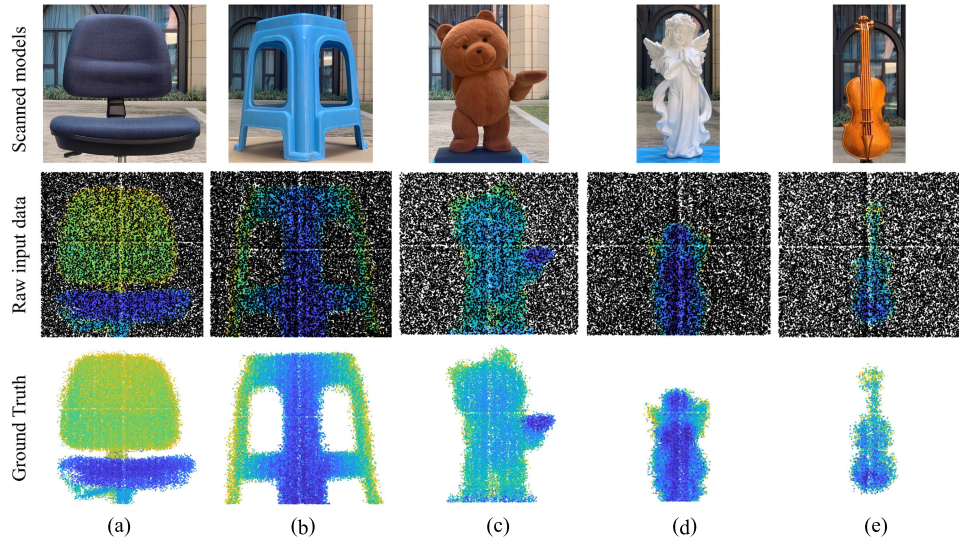


Fig. 8. Models of the scanned data. (a) Chair. (b) Stool. (c) Teddy. (d) Statue. (e) Violin.

| TABLE II PARAMETERS OF ALL EXPERIMENTAL DATA | | |
|---|--------|------------------|
| Models | Points | noise proportion |
| Airplane1 | 9511 | 31.27% |
| Airplane2 | 10559 | 31.17% |
| Airplane3 | 11937 | 29.59% |
| Airplane4 | 8696 | 28.21% |
| Chair | 97717 | 33.43% |
| Stool | 75541 | 42.29% |
| Teddy | 45124 | 50.15% |
| Statue | 45067 | 62.00% |
| Violin | 30895 | 79.16% |

obtained from these two methods, and Local density faces a notable challenge in maintaining features. PointCleanNet's denoising results show minimal presence of noise points. The outcomes from Noniterative, MCMD, and FDID methods closely resemble each other, all retaining varying proportions of noise points. CIMD and LCLOF produce results with fewer noise points and well-preserved features.

The denoising performance evaluation results of various methods are presented in Table III. As depicted in the table, Local density demonstrates unsatisfactory outcomes across all evaluation indicators. SOR exhibits better performance compared to Local density; however, the average values of ODR and Recall are only 0.8427 and 0.8884, respectively. These results emphasize the challenge of achieving significant denoising effects solely based on statistical or density differences among nearest neighbors. PointCleanNet demonstrates

superior noise removal results for different types of synthetic data, with an average ODR of 0.9991, although its average Recall is only 0.8677. This highlights that PointCleanNet struggles to effectively balance denoising ability and feature retention capacity when distribution characteristics vary between test and training point clouds. Since the significant differences in the characteristics of noise and ground truth in synthetic point clouds, the performance evaluation results for the remaining five methods exhibit minor differences. However, due to the advantages of the completion strategies, both CIMD and LCLOF exhibit the best performance, with average accuracies of 0.9964 and 0.9965, respectively.

C. Performance Evaluation on SPAD-Acquired Data

Figs. 13–17 show the visual qualitative comparison of different methods on SPAD-acquired data. We can see that the results of the PointCleanNet are close to the noisy input point clouds. The degraded performance of the PointCleanNet is due to the fact that its pretrained model is trained by the synthetic datasets, and poor generalization ability makes learning-based methods unable to process the SPAD-acquired data directly with pretrained model. The performance of SOR and Local density are relatively poor for these five models. A huge number of isolated noise points still exist in the results processed by these methods. The strategy of SOR will fail when facing the point clouds with a higher noise proportion. For the violin model, truth and noise points are removed

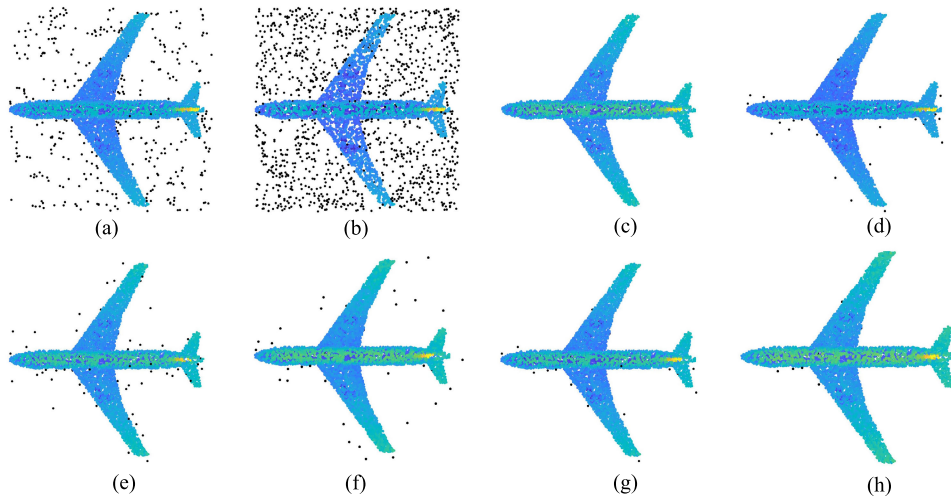


Fig. 9. Denoised results of the Airplane1 model. (a) SOR. (b) Local density. (c) PointCleanNet. (d) Noniterative. (e) MCMD. (f) FCID. (g) CIMD. (h) LCLOF.

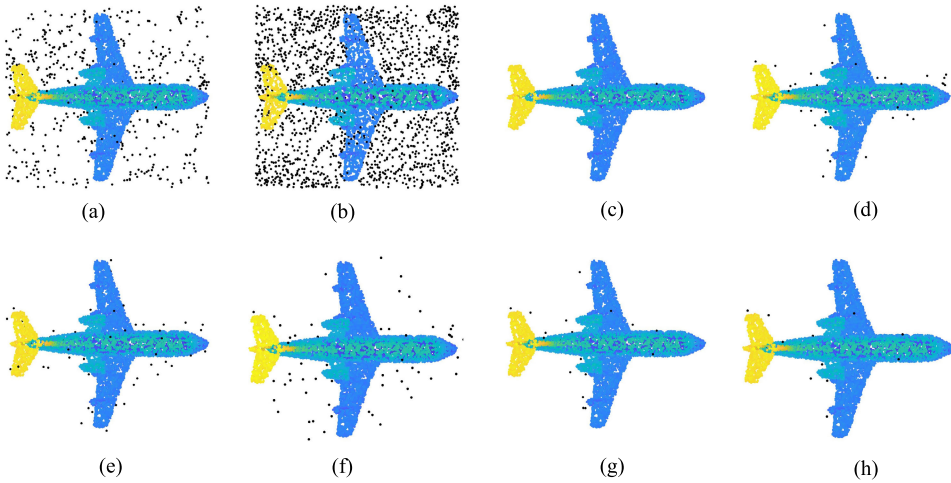


Fig. 10. Denoised results of the Airplane2 model. (a) SOR. (b) Local density. (c) PointCleanNet. (d) Noniterative. (e) MCMD. (f) FCID. (g) CIMD. (h) LCLOF.

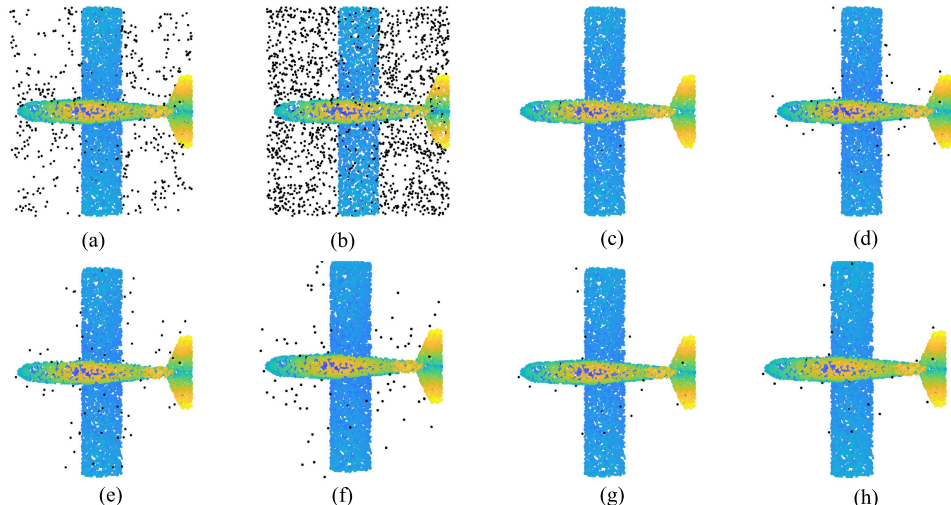


Fig. 11. Denoised results of the Airplane3 model. (a) SOR. (b) Local density. (c) PointCleanNet. (d) Noniterative. (e) MCMD. (f) FCID. (g) CIMD. (h) LCLOF.

together by SOR since it cannot distinguish them. On the contrary, the performance of the local density method does not decrease as the proportion of noise increases, but its processing results still have a large gap compared with the ground truth.

Noniterative and MCMD demonstrate improved efficacy on SPAD-acquired data, but some noise points still surround the ground truth in the outcomes. Notably, CIMD's denoising performance on SPAD-acquired data is weaker compared to its

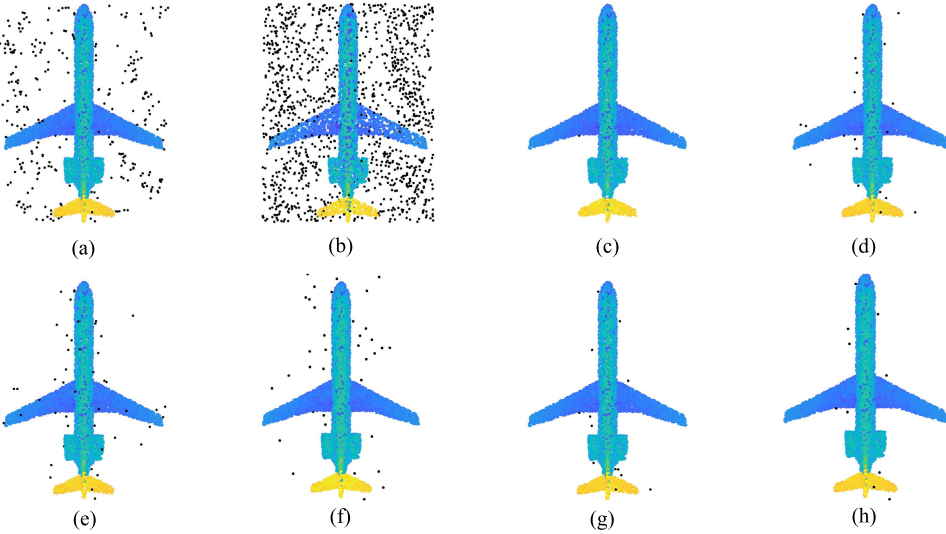


Fig. 12. Denoised results of the Airplane4 model. (a) SOR. (b) Local density. (c) PointCleanNet. (d) Noniterative. (e) MCMD. (f) FCID. (g) CIMD. (h) LCLOF.

TABLE III

PERFORMANCE EVALUATION RESULTS ON SYNTHETIC DATA (HIGHER IS BETTER). NUMBERS IN BOLD ARE THE BEST IN THE ROW, AND NUMBERS IN ITALIC ARE THE SECOND BEST

| Models | Metrics | SOR | Local density | PointCleanNet | Noniterative | MCMD | FCID | CIMD | LCLOF |
|-----------|-----------------|--------|---------------|---------------|---------------|--------|--------|---------------|---------------|
| Airplane1 | <i>ODR</i> | 0.8315 | 0.4518 | 0.9996 | 0.9893 | 0.9759 | 0.9866 | 0.9921 | 0.9962 |
| | <i>Recall</i> | 0.8685 | 0.5021 | 0.8803 | 0.9958 | 0.9827 | 0.9862 | 0.9942 | 0.9931 |
| | <i>Accuracy</i> | 0.9079 | 0.6885 | 0.9574 | 0.9953 | 0.9871 | 0.9915 | 0.9957 | 0.9966 |
| Airplane2 | <i>ODR</i> | 0.8423 | 0.4501 | 0.9994 | 0.9875 | 0.9809 | 0.9809 | 0.9921 | 0.9945 |
| | <i>Recall</i> | 0.8377 | 0.5318 | 0.8773 | 0.9936 | 0.9896 | 0.9878 | 0.9991 | 0.9991 |
| | <i>Accuracy</i> | 0.9001 | 0.7051 | 0.9562 | 0.9941 | 0.9908 | 0.9902 | 0.9973 | 0.9981 |
| Airplane3 | <i>ODR</i> | 0.8347 | 0.4615 | 0.9983 | 0.9858 | 0.9737 | 0.9757 | 0.9901 | 0.9901 |
| | <i>Recall</i> | 0.8551 | 0.5057 | 0.8341 | 0.9820 | 0.9424 | 0.9704 | 0.9949 | 0.9887 |
| | <i>Accuracy</i> | 0.919 | 0.7072 | 0.9407 | 0.9904 | 0.9746 | 0.9841 | 0.9956 | 0.9937 |
| Airplane4 | <i>ODR</i> | 0.8626 | 0.4456 | 0.9988 | 0.9894 | 0.9735 | 0.9837 | 0.9918 | 0.9939 |
| | <i>Recall</i> | 0.9925 | 0.4507 | 0.8791 | 0.9967 | 0.9896 | 0.9877 | 0.9979 | 0.9984 |
| | <i>Accuracy</i> | 0.9594 | 0.6904 | 0.9609 | 0.9961 | 0.9897 | 0.9921 | 0.9971 | 0.9978 |
| Average | <i>ODR</i> | 0.8427 | 0.4522 | 0.9991 | 0.9881 | 0.9761 | 0.9817 | 0.9915 | 0.9937 |
| | <i>Recall</i> | 0.8884 | 0.4975 | 0.8677 | 0.9921 | 0.9761 | 0.9831 | 0.9965 | 0.9948 |
| | <i>Accuracy</i> | 0.9216 | 0.6978 | 0.9538 | 0.9939 | 0.9855 | 0.9894 | 0.9964 | 0.9965 |

performance on synthetic data. This is predominantly due to the complex attributes of SPAD-acquired point clouds, where relying solely on the completion strategy fails to achieve superior denoising outcomes. FCID achieves good denoising effects on SPAD-acquired point clouds with the consideration of laser detection characteristics and multiiteration noise detection. However, its denoised results lose some edge features. In comparison to FDID, our method preserves structural details, and the remaining noise points are primarily clustered around the edges of the surface, largely due to errors in manual labeling. These figures collectively demonstrate that the proposed method yields superior visual results compared to other methods, particularly in terms of noise point removal and preservation of geometric features.

The ODR and Recall results for the eight methods are presented in Tables IV and V. The PointCleanNet method displays inadequate performance across all models. It is noteworthy that Recall values for PointCleanNet are higher for the Statue and Violin models; however, PointCleanNet exhibits the lowest rate of noise point removal. This disparity arises because PointCleanNet removes only a small number of points, most of which are truth points. For the Chair model with a noise

proportion of 33.43%, SOR and Local density achieve ODR values of 0.7035 and 0.5486, respectively, accompanied by Recall values of 0.7105 and 0.5613, respectively. Conversely, for the Violin model with a noise proportion of 79.16%, SOR, and Local density yield ODR values of 0.1063 and 0.8778, respectively, along with Recall values of 0.3180 and 0.8879, respectively. Therefore, SOR proves effective for processing point clouds characterized by low noise proportions, whereas Local density outperforms SOR for point clouds featuring higher noise proportions. Noniterative, MCMD, and CIMD methods consistently exhibit better performance across all models. Among them, CIMD consistently secures the second-best position in these tables, achieving an average ODR of 0.9784 and Recall of 0.9826. However, considering the distribution of remaining noise points in the visual results, the outcomes of these three methods are still unsatisfactory for practical applications. As a denoising approach that also takes into account SPAD detection characteristics, the proposed method outperforms the FCID method significantly in the performance evaluation results for all models. Table VI displays the Accuracy results for the eight methods. Notably, the proposed method boasts the highest average Accuracy

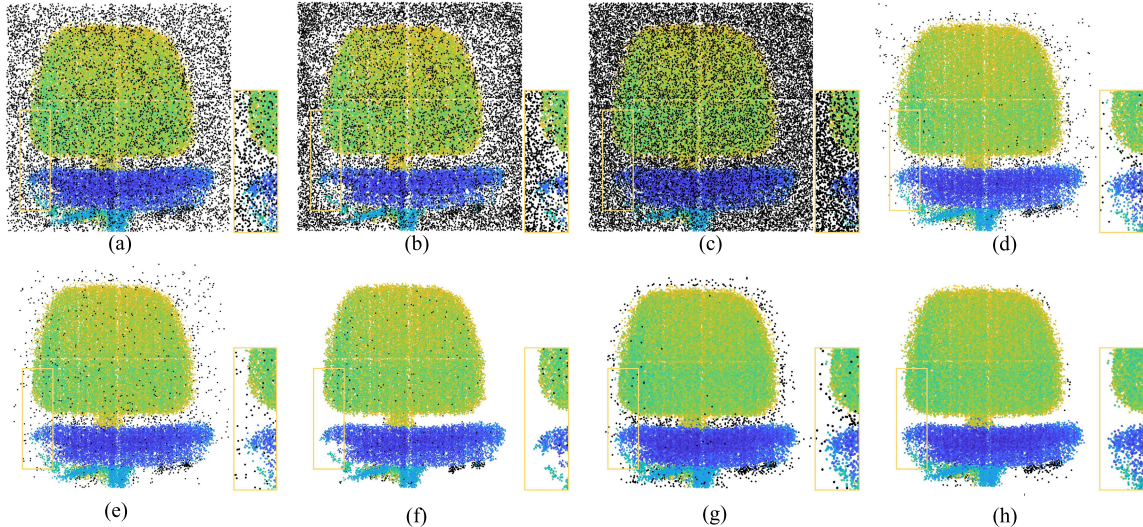


Fig. 13. Denoised results of the Chair model. (a) SOR. (b) Local density. (c) PointCleanNet. (d) Noniterative. (e) MCMD. (f) FCID. (g) CIMD. (h) LCLOF.

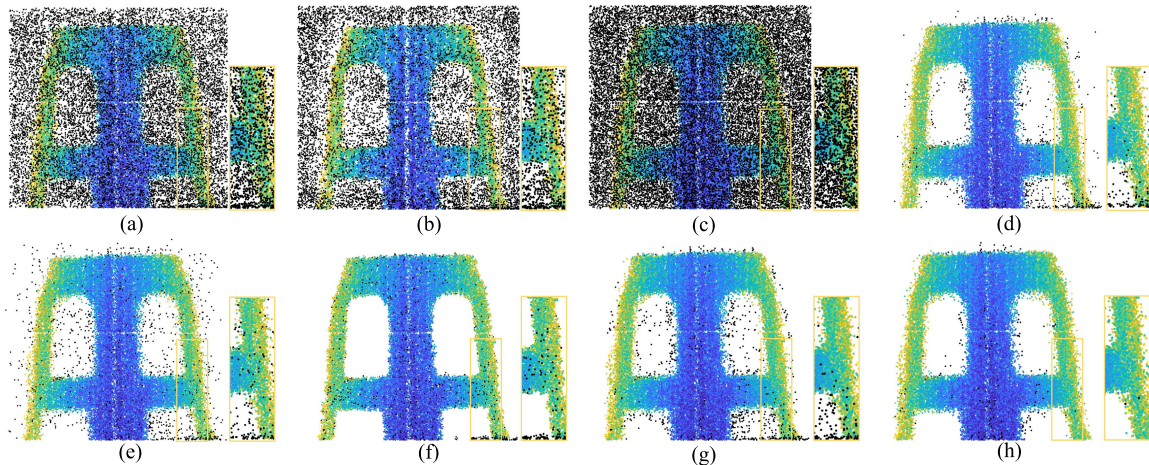


Fig. 14. Denoised results of the Stool model. (a) SOR. (b) Local density. (c) PointCleanNet. (d) Noniterative. (e) MCMD. (f) FCID. (g) CIMD. (h) LCLOF.

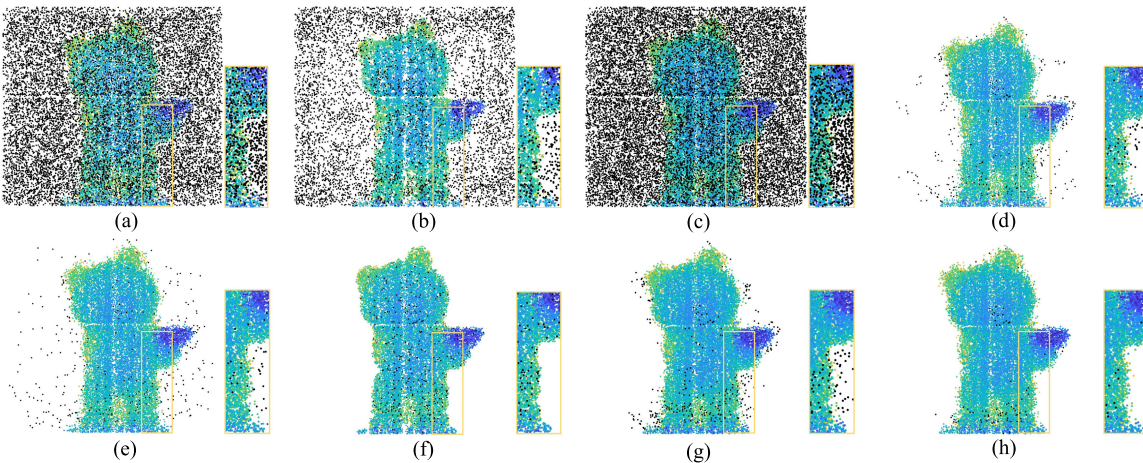


Fig. 15. Denoised results of the Teddy model. (a) SOR. (b) Local density. (c) PointCleanNet. (d) Noniterative. (e) MCMD. (f) FCID. (g) CIMD. (h) LCLOF.

of 0.9918, affirming its superior performance when handling real-world scanned data.

D. Ablation Study

We conduct the ablation studies on the Teddy model to demonstrate the effectiveness of LCLOF's three components.

1) Remove Rough-Denoising: This unit preprocesses the input raw point clouds to filter the majority of isolated noise points. After removing rough-denoising, we directly input the raw point clouds into the over-denoising module. Feature points are defined as the differences between the raw point clouds and the incomplete point clouds.

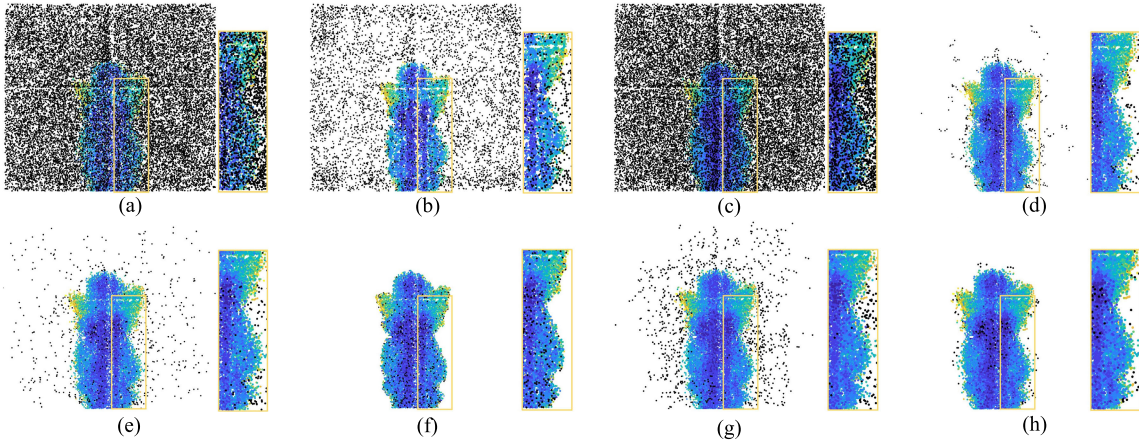


Fig. 16. Denoised results of the Statue model. (a) SOR. (b) Local density. (c) PointCleanNet. (d) Noniterative. (e) MCMD. (f) FCID. (g) CIMD. (h) LCLOF.

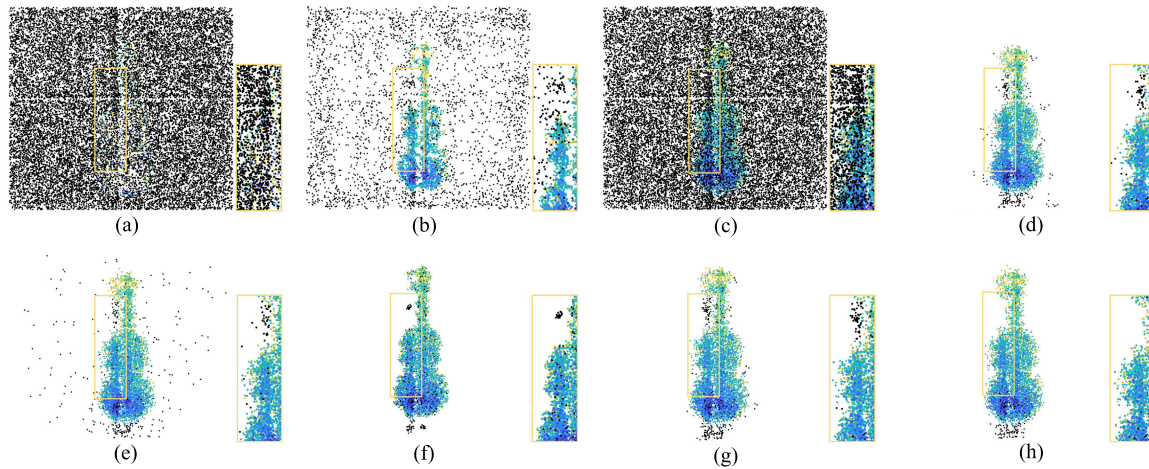


Fig. 17. Denoised results of the Violin model. (a) SOR. (b) Local density. (c) PointCleanNet. (d) Noniterative. (e) MCMD. (f) FCID. (g) CIMD. (h) LCLOF.

TABLE IV
PERFORMANCE EVALUATION RESULTS OF ODR ON SCANNED DATA (HIGHER IS BETTER). NUMBERS IN BOLD
ARE THE BEST IN THE ROW, AND NUMBERS IN ITALIC ARE THE SECOND BEST

| Models | SOR | Local density | PointCleanNet | Noniterative | MCMD | FCID | CIMD | LCLOF |
|---------|--------|---------------|---------------|---------------|--------|---------------|--------|---------------|
| Chair | 0.7035 | 0.5486 | 0.2446 | 0.9727 | 0.9697 | 0.9795 | 0.9718 | 0.9877 |
| Stool | 0.5608 | 0.6439 | 0.2117 | 0.9793 | 0.9701 | 0.9699 | 0.9756 | 0.9907 |
| Teddy | 0.4231 | 0.7251 | 0.1829 | 0.9872 | 0.9852 | 0.9816 | 0.9857 | 0.9946 |
| Statue | 0.2526 | 0.8174 | 0.1728 | 0.9867 | 0.9791 | 0.9814 | 0.9677 | 0.9942 |
| Violin | 0.1063 | 0.8778 | 0.1298 | 0.9905 | 0.9886 | 0.9873 | 0.9912 | 0.9947 |
| Average | 0.4092 | 0.7225 | 0.1883 | 0.9832 | 0.9785 | 0.9799 | 0.9784 | 0.9924 |

TABLE V
PERFORMANCE EVALUATION RESULTS OF RECALL ON SCANNED DATA (HIGHER IS BETTER)

| Models | SOR | Local density | PointCleanNet | Noniterative | MCMD | FCID | CIMD | LCLOF |
|---------|--------|---------------|---------------|--------------|--------|--------|---------------|---------------|
| Chair | 0.7105 | 0.5613 | 0.6952 | 0.9718 | 0.9548 | 0.9773 | 0.9791 | 0.9808 |
| Stool | 0.6006 | 0.6777 | 0.8475 | 0.9781 | 0.9731 | 0.9734 | 0.9828 | 0.9904 |
| Teddy | 0.5188 | 0.7331 | 0.9303 | 0.9812 | 0.9632 | 0.9782 | 0.9881 | 0.9917 |
| Statue | 0.4504 | 0.8326 | 0.9941 | 0.9838 | 0.9841 | 0.9882 | 0.9707 | 0.9914 |
| Violin | 0.3181 | 0.8879 | 0.9975 | 0.9922 | 0.9879 | 0.9893 | 0.9925 | 0.9968 |
| Average | 0.5196 | 0.7385 | 0.8929 | 0.9814 | 0.9725 | 0.9812 | 0.9826 | 0.9902 |

2) Remove Over-Denoising: This unit further denoises the rough point clouds to obtain the incomplete point clouds. After removing this unit, the incomplete point clouds are directly generated by the rough-denoising. Feature points are defined as the differences between the raw point clouds and the incomplete point clouds.

3) Remove Point Clouds Completion: This unit filters feature points based on ILOF and fills the selected points back into the incomplete point clouds. After removing this unit, we rely solely on rough-denoising and over-denoising for point cloud processing, i.e., we do not perform completion as in our original LCLOF.

TABLE VI
PERFORMANCE EVALUATION RESULTS OF ACCURACY ON SCANNED DATA (HIGHER IS BETTER)

| Models | SOR | Local density | PointCleanNet | Noniterative | MCMD | FCID | CIMD | LCLOF |
|---------|--------|---------------|---------------|---------------|--------|--------|--------|---------------|
| Chair | 0.8051 | 0.7058 | 0.7116 | 0.9814 | 0.9744 | 0.9855 | 0.9837 | 0.9894 |
| Stool | 0.6566 | 0.7199 | 0.6505 | 0.9821 | 0.9761 | 0.9761 | 0.9825 | 0.9921 |
| Teddy | 0.5139 | 0.7297 | 0.5834 | 0.9841 | 0.9737 | 0.9798 | 0.9868 | 0.9931 |
| Statue | 0.3455 | 0.7849 | 0.4865 | 0.9816 | 0.9771 | 0.9812 | 0.9619 | 0.9911 |
| Violin | 0.1121 | 0.8156 | 0.3109 | 0.9863 | 0.9814 | 0.9815 | 0.9871 | 0.9933 |
| Average | 0.4866 | 0.7511 | 0.5485 | 0.9831 | 0.9765 | 0.9808 | 0.9804 | 0.9918 |

TABLE VII
PERFORMANCE EVALUATION OF ALL ABLATED METHODS BASED
ON OUR ORIGINAL LCLOF (HIGHER IS BETTER)

| | ODR | Recall | Accuracy |
|--------------------------------|---------------|---------------|---------------|
| Remove rough-denoising | 0.9901 | 0.9892 | 0.9896 |
| Remove over-denoising | 0.9918 | 0.9907 | 0.9912 |
| Remove point clouds completion | 0.9906 | 0.9860 | 0.9882 |
| Replace with LOF | 0.9785 | 0.9771 | 0.9777 |
| The full framework | 0.9946 | 0.9917 | 0.9931 |

4) *Replace With LOF*: ILOF considers the density correlation between the incomplete point clouds and feature points to finish the feature point filtering. When replaced with LOF, feature point filtering is performed based on the union of the incomplete point clouds and feature points, i.e., the rough point clouds. As a result, its performance may be comparatively poorer.

Table VII compares the three evaluation metrics of all ablated methods. From the table, we can see that as follows.

- 1) The greatest impact is caused by the replacement with LOF. LOF method filters feature points based on mixed point clouds, which cannot guarantee the extraction of relative density features without being affected by the interference of noise.
- 2) The removal of point cloud completion demonstrates the second major impact on performance, indicating that this unit is essential for the high-precision identification of noise points and ground truth.
- 3) The removal of rough-denoising or over-denoising results in decreased performance due to the inability to effectively acquire feature points and incomplete point clouds.

From this ablation study, we can observe how the three steps of the proposed LCLOF method complement each other to achieve state-of-the-art performance.

E. Computation Time Cost of Processing

Table VIII presents comparative results of computational speeds for various methods, measured in seconds. The results represent the average computation time over 30 runs for each method. The PointCleanNet method is implemented in Python, and all other methods are implemented in MATLAB. As demonstrated in Table VII, The noniterative method exhibits notably shorter computation times compared to other techniques. This can be attributed to the fact that Noniterative directly detects noise based on the spatial similarity, without considering the search steps for neighboring points. SOR and Local density exhibit similar computation speeds. Their expeditious calculation can be attributed to single-stage processing, which lead to the loss of denoising performance.

PointCleanNet displays the longest average computation time. The point-by-point feature extraction and fusion contribute to its higher computational overhead when processing large point clouds. MCMD and FCID both employ an iterative search strategy for denoising, enhancing denoising accuracy but also introducing additional computational costs. Compared to CIMD, the proposed method showcases a relatively lower runtime, despite both methods employing completion denoising strategies. The inclusion of a discrete detection probabilistic model and ILOF enhances the denoising performance of the proposed method, while a simplified preprocessing architecture significantly reduces computation time.

F. Parameter Selection and Tuning

The proposed method encompasses specific relevant parameters that wield substantial influence over its performance, analogous to other denoising methods. Provided below are recommendations for parameter selection.

1) *Nearest Neighbors' Size*: Rough-denoising, over-denoising, and point cloud completion operations include this parameter. This parameter's selection should correspond to the noise statistical characteristics inherent in the input data. During the rough-denoising procedure, it is advisable to opt for a higher value for the nearest neighbors (k_1), given the considerable noise prevalence in the input noisy point clouds. Conversely, for over-denoising and point cloud completion steps, it is recommended to assign smaller values to parameters k_2 and k_3 , considering the relatively lower noise proportion in the remaining point clouds. Suitable values usually lie within the range of [2, 50].

2) *Score Threshold*: The score threshold ψ is used to filter the mean value of trigger probabilities for the isolated noise points removal operation. Reasonable values are within $[10^{-6}, 10^{-8}]$.

3) *Bounding Threshold*: The bounding threshold w is utilized to control the extent to which the side length of the bounding box is influenced by the triggering probability. Reasonable values are within [0.1, 0.8].

4) *ILOF Threshold*: The ILOF threshold δ will determine whether the feature point screening is strict. Smaller values will result in the removal of more points, whereas larger values will retain more fine-grained detail features. Reasonable values are within [0.3, 1].

Our previous work has provided an evolutionary computation-based parameter optimization method for point clouds denoising [37]. Based on the reasonable values of each parameter, the specific parameter configurations for LCLOF concerning different experimental scenarios can be automatically obtained using the parameter optimization

TABLE VIII

COMPUTATION TIME COST (IN SECONDS) FOR DIFFERENT MODELS (LOWER IS BETTER)

| Models | SOR | Local density | PointCleanNet | Noniterative | MCMD | FCID | CIMD | LCLOF |
|---------|--------|---------------|---------------|---------------|---------|----------|---------|--------|
| Chair | 0.3581 | 0.6146 | 408.8477 | 0.0185 | 20.8175 | 412.5878 | 34.4932 | 3.7792 |
| Stool | 0.2717 | 0.4701 | 258.3082 | 0.0111 | 15.6962 | 168.0501 | 19.0362 | 2.0221 |
| Teddy | 0.1561 | 0.2635 | 85.1625 | 0.0061 | 9.5098 | 36.2455 | 2.7247 | 0.9914 |
| Statue | 0.1553 | 0.2692 | 69.5513 | 0.0056 | 9.7054 | 35.8784 | 3.2515 | 0.8921 |
| Violin | 0.1055 | 0.1785 | 24.3683 | 0.0026 | 6.4045 | 8.6756 | 0.9826 | 0.4278 |
| Average | 0.2093 | 0.3591 | 169.2476 | 0.0087 | 12.4266 | 132.287 | 12.0976 | 1.6225 |

strategy. Specifically, the optimization process commences with an initialization phase, where multiple parameter sets are generated randomly within the range of the provided reasonable values. Subsequently, LCLOF employs these parameter sets to denoise the input point clouds, resulting in denoised point clouds. The quality of denoised point clouds is quantitatively assessed via no-reference objective functions, with their evaluation results as fitness values for each parameter set. The evolutionary computation algorithm updates these parameter sets in accordance with their fitness values and the optimization strategy. The updated parameters are then fed back into the LCLOF. The optimization process continues until a maximum number of iterations is reached, culminating in the identification of the most suitable LCLOF parameter configuration for the given point clouds.

VI. CONCLUSION

We propose a novel point cloud denoising method called LCLOF based on the completion denoising strategy and the SPAD discrete probability model. The proposed method starts by processing the raw input data to generate rough point clouds. This step is accomplished using the full noise point cloud, Lider equation, and the SPAD discrete probability model. The incomplete point clouds are then obtained by performing an improved layered method on the rough point clouds considering the detection characteristics of SPAD. The differences between incomplete point clouds and rough point clouds are treated as feature points, which are filtered by the ILOF strategy. The filtered feature points are utilized to populate the incomplete point clouds, ultimately finalizing the point cloud denoising process. Theoretical analysis confirms that the ILOF technique is appropriate for evaluating point clouds that exhibit nonuniform density. Experimental results show that on the synthetic data and the real-world data, LCLOF excels in comparison to state-of-the-art approaches, delivering superior results in denoising precision and the retention of intricate features.

REFERENCES

- [1] Y. Li, H. Fu, J. Zhu, L. Wang, R. Zhao, and C. Wang, "A photon cloud filtering method in forested areas considering the density difference between canopy photons and ground photons," *IEEE Trans. Geosci. Remote Sens.*, vol. 61, 2023, Art. no. 4403114.
- [2] S. Li, J. Zhao, H. Zhang, Q. Gong, Z. Bi, and S. Qu, "Surface extraction and segmentation from 3-D underwater sub-bottom point clouds using enhancement filtering and global energy optimization," *IEEE Trans. Geosci. Remote Sens.*, vol. 60, 2022, Art. no. 5907814.
- [3] E. P. McShane et al., "High resolution TCSPC imaging of diffuse light with a one-dimensional SPAD array scanning system," *Opt. Exp.*, vol. 30, no. 15, pp. 27926–27937, 2022.
- [4] S. Huang and M. Safari, "SPAD-based optical wireless communication with signal pre-distortion and noise normalization," *IEEE Trans. Commun.*, vol. 70, no. 4, pp. 2593–2605, Apr. 2022.
- [5] J. Long, H. Zhang, and J. Zhao, "A comprehensive deep learning-based outlier removal method for multibeam bathymetric point cloud," *IEEE Trans. Geosci. Remote Sens.*, vol. 61, 2023, Art. no. 4201622.
- [6] F. Yang, F. Xu, M. Fan, X. Bu, Z. Tu, and X. Yan, "An intelligent detection method for different types of outliers in multibeam bathymetric point cloud," *IEEE Trans. Geosci. Remote Sens.*, vol. 60, 2022, Art. no. 5920710.
- [7] Y. Li and H. Sheng, "A single-stage point cloud cleaning network for outlier removal and denoising," *Pattern Recognit.*, vol. 138, Jun. 2023, Art. no. 109366.
- [8] H. Yan, L. Wang, and Y. Lu, "Identifying cluster centroids from decision graph automatically using a statistical outlier detection method," *Neurocomputing*, vol. 329, pp. 348–358, Feb. 2019.
- [9] L. Zhou, G. Sun, Y. Li, W. Li, and Z. Su, "Point cloud denoising review: From classical to deep learning-based approaches," *Graph. Models.*, vol. 121, May 2022, Art. no. 101140.
- [10] Z. Feng et al., "Fast depth imaging denoising with the temporal correlation of photons," *IEEE Photon. J.*, vol. 9, no. 5, pp. 1–10, Oct. 2017.
- [11] C. Qu, Y. Zhang, K. Huang, S. Wang, and Y. Yang, "Point clouds outlier removal method based on improved Mahalanobis and completion," *IEEE Robot. Autom. Lett.*, vol. 8, no. 1, pp. 17–24, Jan. 2023.
- [12] C. Qu, Y. Zhang, Y. Yang, and S. Wang, "Discrete probabilistic detection model for a geiger-mode avalanche photodiode array with crosstalk," *Opt. Lett.*, vol. 46, no. 6, p. 1442, Mar. 15, 2021.
- [13] H. Balta, J. Velagic, H. Beglerovic, G. De Cubber, and B. Siciliano, "3D registration and integrated segmentation framework for heterogeneous unmanned robotic systems," *Remote Sens.*, vol. 12, no. 10, p. 1608, May 2020.
- [14] M. Salehi, C. Leckie, J. C. Bezdek, T. Vaithianathan, and X. Zhang, "Fast memory efficient local outlier detection in data streams," *IEEE Trans. Knowl. Data Eng.*, vol. 28, no. 12, pp. 3246–3260, Dec. 2016.
- [15] L. Chen, W. Wang, and Y. Yang, "CELOF: Effective and fast memory efficient local outlier detection in high-dimensional data streams," *Appl. Soft Comput.*, vol. 102, Apr. 2021, Art. no. 107079.
- [16] X. Ning, F. Li, G. Tian, and Y. Wang, "An efficient outlier removal method for scattered point cloud data," *PLoS ONE*, vol. 13, no. 8, Aug. 2018, Art. no. e0201280.
- [17] S. Zhou, X. Liu, C. Wang, and B. Yang, "Non-iterative denoising algorithm based on a dual threshold for a 3D point cloud," *Opt. Lasers Eng.*, vol. 126, Mar. 2020, Art. no. 105921.
- [18] P. Huang, W. He, G. Gu, and Q. Chen, "Depth imaging denoising of photon-counting LiDAR," *Appl. Opt.*, vol. 58, no. 16, p. 4390, Jun. 2019.
- [19] W. He et al., "Adaptive depth imaging with single-photon detectors," *IEEE Photon. J.*, vol. 9, no. 2, pp. 1–12, Apr. 2017.
- [20] F. Zhang, C. Zhang, H. Yang, and L. Zhao, "Point cloud denoising with principal component analysis and a novel bilateral filter," *Traitemen Signal*, vol. 36, no. 5, pp. 393–398, Nov. 2019.
- [21] X.-F. Han, J. S. Jin, M.-J. Wang, and W. Jiang, "Guided 3D point cloud filtering," *Multimedia Tools Appl.*, vol. 77, no. 13, pp. 17397–17411, Jul. 2018.
- [22] X.-F. Han, J. S. Jin, M.-J. Wang, and W. Jiang, "Iterative guidance normal filter for point cloud," *Multimedia Tools Appl.*, vol. 77, no. 13, pp. 16887–16902, Jul. 2018.
- [23] C. Dinesh, G. Cheung, and I. V. Bajic, "Point cloud denoising via feature graph Laplacian regularization," *IEEE Trans. Image Process.*, vol. 29, pp. 4143–4158, 2020.
- [24] C. Lv, W. Lin, and B. Zhao, "Approximate intrinsic Voxel structure for point cloud simplification," *IEEE Trans. Image Process.*, vol. 30, pp. 7241–7255, 2021.

- [25] R. Preiner, O. Mattausch, M. Arikan, R. Pajarola, and M. Wimmer, "Continuous projection for fast L-1 reconstruction," *ACM Trans. Graph.*, vol. 33, no. 4, pp. 1–13, Jul. 2014.
- [26] H. Liu, L. Li, J. Lu, and S. Tan, "Group sparsity mixture model and its application on image denoising," *IEEE Trans. Image Process.*, vol. 31, pp. 5677–5690, 2022.
- [27] H. Chen, M. Wei, Y. Sun, X. Xie, and J. Wang, "Multi-patch collaborative point cloud denoising via low-rank recovery with graph constraint," *IEEE Trans. Vis. Comput. Graphics*, vol. 26, no. 11, pp. 3255–3270, Nov. 2020.
- [28] D. Zhu et al., "Nonlocal low-rank point cloud denoising for 3-D measurement surfaces," *IEEE Trans. Instrum. Meas.*, vol. 71, pp. 1–14, 2022.
- [29] M. Rakotosaona, V. La Barbera, P. Guerrero, N. J. Mitra, and M. Ovsjanikov, "PointCleanNet: Learning to denoise and remove outliers from dense point clouds," *Comput. Graph. Forum*, vol. 39, no. 1, pp. 185–203, Feb. 2020.
- [30] D. Zhang, X. Lu, H. Qin, and Y. He, "PointFilter: Point cloud filtering via encoder-decoder modeling," *IEEE Trans. Vis. Comput. Graph.*, vol. 27, no. 3, pp. 2015–2027, Mar. 2021.
- [31] K. Morimoto et al., "Megapixel time-gated SPAD image sensor for 2D and 3D imaging applications," *Optica*, vol. 7, no. 4, pp. 346–354, Apr. 2020.
- [32] M.-A. Tétrault et al., "Real-time discrete SPAD array readout architecture for time of flight PET," *IEEE Trans. Nucl. Sci.*, vol. 62, no. 3, pp. 1077–1082, Jun. 2015.
- [33] I. Gyongy et al., "High-speed 3D sensing via hybrid-mode imaging and guided upsampling," *Optica*, vol. 7, no. 10, p. 1253, Oct. 20, 2020.
- [34] D. G. Fouche, "Detection and false-alarm probabilities for laser radars that use geiger-mode detectors," *Appl. Opt.*, vol. 42, no. 27, p. 5388, Sep. 20, 2003.
- [35] X. Yuan, H. Chen, and B. Liu, "Point cloud clustering and outlier detection based on spatial neighbor connected region labeling," *Meas. Control*, vol. 54, nos. 5–6, pp. 835–844, May 2021.
- [36] Z. Gao, Y. Zhang, H. Zhang, W. Guan, D. Feng, and S. Chen, "Multi-level view associative convolution network for view-based 3D model retrieval," *IEEE Trans. Circuits Syst. Video Technol.*, vol. 32, no. 4, pp. 2264–2278, Apr. 2022.
- [37] C. Qu, Y. Zhang, F. Ma, and K. Huang, "Parameter optimization for point clouds denoising based on no-reference quality assessment," *Measurement*, vol. 211, Apr. 2023, Art. no. 112592.



Chengzhi Qu received the B.S. degree in automation and the M.S. degree in control engineering from the Shandong University of Science and Technology, Qingdao, China, in 2016 and 2019, respectively, and the Ph.D. degree in aeronautical and astronautical science and technology from Sun Yat-sen University, Shenzhen, China, in 2023.

He is currently a Lecturer with the School of Artificial Intelligence, Nanjing University of Information Science and Technology, Nanjing, China. His main research interests include computer vision, evolutionary computation, and parameter optimization.



Yan Zhang received the B.S. degree in aerodynamics, the M.S. degree in mechanics, and the Ph.D. degree in aeronautical and astronautical science and technology from the National University of Defense Technology, Changsha, China, in 1998, 2001, and 2005, respectively.

She is currently a Professor with the School of Electronics and Communication Engineering, Sun Yat-sen University, Shenzhen, China. Her main research interests include computer vision, information fusion, and pattern recognition.



Ziwen Sun received the B.S. degree in nuclear engineering and technology and the M.S. degree in nuclear energy and nuclear technology engineering from Sun Yat-sen University, Zhuhai, China, in 2016 and 2018, respectively. He is currently pursuing the Ph.D. degree in aeronautical and astronautical science and technology with Sun Yat-sen University, Shenzhen, China.

His research interests include compressive sensing, sparse representation, and flight control.



Feifan Ma received the B.S. degree in aeronautical and astronautical engineering from Sun Yat-sen University, Shenzhen, China, in 2012, where he is currently pursuing the Ph.D. degree in aeronautical and astronautical science and technology with the School of Aeronautics and Astronautics.

His research interests include computer vision and pattern recognition.



Xin Zhang received the B.S. degree in mathematics from Nanjing Agricultural University, Nanjing, China, in 2019, and the M.S. degree in aerospace and astronautics from Sun Yat-sen University, Shenzhen, China, in 2022.

She is currently an Engineer with the Shanghai Satellite Engineering Institute, Shanghai, China. Her main research interests include computer vision and embedded software development.